

Prediction of UH-60 Main Rotor Structural Loads using CFD/Comprehensive Analysis Coupling

Anubhav Datta
datta@eng.umd.edu
Asst. Research Scientist

Inderjit Chopra
chopra@eng.umd.edu
Alfred Gessow Professor

Department of Aerospace Engineering
University of Maryland, College Park, MD 20742

ABSTRACT

This paper studies the predicted UH-60A main rotor structural loads using Computational Fluid Dynamics (CFD) and Computational Structural Dynamics (CSD) coupling. The accuracy of the CSD model by itself is studied by using the flight test measured airloads, damper force and control angles. The CFD/CSD predictions are then compared with flight test data and predictions using measured airloads at three level flight conditions. The flight conditions are each characterized by different aerodynamic phenomena - wake at low speed, unsteady transonic pitching moments at high speed, and dynamic stall cycles at high altitude. Each flight is also characterized by a different structural dynamic phenomena - 3/rev flap bending at low speed, low frequency elastic twist (1,2/rev) at high speed, and high frequency elastic twist at stall. The predicted flap bending moments are satisfactory at high speed; show a 3/rev phase error in stall, and up-to 50% under-prediction of 3/rev magnitude at low speed. The problem appears to stem from the predicted airloads. The predicted torsion loads are satisfactory up to 3/rev. The 4/rev and higher harmonics show significant discrepancies (up to 50% error with test data). The problem appears to stem from structural dynamics. The predicted chord bending moments show significant discrepancies in the magnitudes of 4 and 5/rev harmonics. On an average, the 4/rev is under-predicted by 50% and the 5/rev is over-predicted by 50% along the span.

INTRODUCTION

This paper predicts and validates the UH-60A main rotor structural dynamic loads in three critical level flight conditions. They are the low speed transition flight, Counter 8513 (C8513) (advance ratio $\mu = 0.153$, thrust coefficient $C_T/\sigma = 0.076$, vehicle weight coefficient $C_W/\sigma = 0.0783$), the moderate speed high altitude flight C9017 ($\mu = 0.237$, $C_T/\sigma = 0.129$, $C_W/\sigma = 0.135$), and the high speed flight C8534 ($\mu = 0.368$, $C_T/\sigma = 0.084$, $C_W/\sigma = 0.0783$). The low and high speed flights are the two highest vibration regimes [1]. High vibration is associated with high direct operating cost of a helicopter. The

high altitude stalled flight is not loads critical in itself. However, it acts as a test case for successful prediction of stall loads which occur during severe maneuvers [2].

There has been a significant improvement in the fundamental understanding and prediction of high speed UH-60A flight test loads [3, 4, 5, 6]. The two barrier problems of peak to peak pitch link load and advancing blade lift phase [1] appear to be better understood. The high speed wind tunnel test airloads for the Onera 7A, and 7AD rotors have been studied and well predicted in Refs. [7, 8, 9]. The focus in these efforts has been on the consistent coupling of rotor comprehensive analyses with RANS CFD, and resolving the 3D unsteady transonic pitching moments near the blade tip. Reference [5] used comprehensive analyses/CFD coupling to study airloads at all critical level flight conditions, including hover. The retreating blade stall cycles were satisfactorily predicted.

Presented at the 32nd European Rotorcraft Forum, Maastricht, The Netherlands, September 12-14, 2006.

Predictions at low speed transition were either similar to or improved from (depending on the radial station) a lifting-line model with free wake. The retreating blade stall cycles were further investigated in detail in Ref. [10]. Both aerodynamic and structural loads were predicted for the high altitude stall flight. Recently, Ref. [11] predicted aerodynamic and structural loads at three level flight conditions.

The focus of the present paper is on assessing the state of the art in the prediction of structural loads in steady flight conditions using CFD/CSD coupling. The present paper would systematically investigate the flap and chord (lag) bending moments, torsion moment, and pitch link loads at the three level flight conditions. Flight test data from the UH-60A Airloads Program flights 8513, 8534, 9017, and will be used for the study. The University of Maryland Advanced Rotorcraft Code (UMARC) will be used as the comprehensive analysis platform [12]. The overset grid based University of Maryland Transonic Unsteady Rotor Navier-Stokes (UMTURNS) analysis will be used as the RANS CFD model for coupling with UMACR [11].

THREE CRITICAL LEVEL FLIGHT CONDITIONS

Figure 1(from Ref. [1]) shows the measured pilot seat vibrations for the UH-60A helicopter. The Intrusion Index is a basic measure of helicopter vibration as given in the Aeronautical Design Standard released in 1986 as ADS-27 by the U.S. Army Aviation Systems Command, AVSCOM. It is computed by normalizing triaxial accelerometer data for the four largest spectral peaks up to 60 Hz, excluding 1/rev [13]. The original standards set by the Utility Tactical Transport Aircraft System (UTTAS) and Advanced Attack Helicopter (AAH) developmental programs, and the revised, less stringent ADS-27 requirements are shown in the figure. The highest vibrations for this helicopter occur in two two level flight conditions: (1) low speed transition (around 40 kts for the UH-60A) and (2) high speed forward flight (above 150 kts for the UH-60A). The rotor flow field in the first regime is characterized by wake induced loadings in the first and fourth quadrants. The rotor flow field in the second regime is characterized by tip compressibility effects on the advancing side, between the first and second quadrants. The two high vibration regimes translate directly to high operating and maintenance costs, and reduced crew and system performance for critical missions.

The limiting design loads, on the other hand, occur during maneuvers under high load dynamic stall conditions, e.g. during symmetrical pull up and diving turns [14]. The two severest maneuvers are shown in figure 2. Wake, compressibility and dynamic stall all play

important roles. Reference [14] showed, that there exist high altitude, moderate speed level flight conditions, where the dynamic stall cycles are similar to those occurring in high load maneuvers. For example, figure 3 compares the sectional aerodynamic pitching moments between the steady level high altitude stall flight and the severest pull-up maneuver. The pull-up maneuver is unsteady and the pitching moment shown is that occurring during the 14-th revolution of the maneuver. The vehicle operates at 2.12g and around 140 kts during this revolution. The pull-up maneuver has an additional advancing blade transonic stall cycle absent in the level flight. The two retreating blade cycles are remarkably similar. A detailed analysis of this flight condition [10] showed that the first retreating blade cycle is a trim stall. The second cycle is primarily a twist stall affected both by inflow and turbulence. The high frequency pitch link load (4/rev and higher) and the resultant swashplate servo loads in the fixed frame are dominated by the stall loads. Together with the low speed and high speed conditions, the high altitude level flight condition forms three important regimes (figure 2).

In each of these regimes, one out of the three key aerodynamic phenomenon are more dominant than the others. Similarly, the key structural dynamic phenomena in each of these regimes are also different. At low speed, the 3/rev flap bending moment is the critical load. At high speed, the low frequency torsion (1 and 2/rev) is the key mechanism. At high altitude stall, the high frequency torsion (4 and 5/rev) are more important. Thus, the three flight conditions are ideally suited for validating the analysis methods separately. For predicting design loads in maneuvering flight, it is necessary to begin with these level flight regimes, understand the mechanisms behind loads and vibration in each, and predict them accurately. This paper presents an assessment of the predicted structural loads at the three flight conditions using CFD/CSD coupling performed at the University of Maryland over the last three years.

COMPARISON OF FLIGHT TEST LOADS AT THE THREE FLIGHTS

Out of the three flights, the high speed flight 8534 has in general the highest structural loads. Figure 4 compares the 1-6/rev flap bending moment magnitudes between the high and low speed flight conditions. The 3/rev is the dominant component at low speed. The vibratory harmonics (3-5/rev) at low speed are in general lower compared to high speed. This is expected from figure 1. The vibration level at advance ratio μ of 0.153 is half of that at μ of 0.368. A nearby flight condition, flight C8515, occurring at μ of 0.110, is a more suitable high vibration test case. This flight condition was studied re-

cently by Ref. [11]. In the present paper, flight C8513 is studied. The azimuthally corrected PDB data set is available for this flight. The same flight was studied earlier by Potsdam et al [5]. Even though it is a relatively low vibration flight compared to C8515, the wake induced vibratory airload mechanism is the same. Similarly the vibratory structural load mechanism is also the same. The 3/rev flap bending moment is the largest vibratory load. Figure 5 compares the torsion loads. The torsion loads at low speed are relatively benign, except the 4/rev harmonic. The chord bending moments are shown in figure 6. Except for the 5/rev harmonic, all loading harmonics are relatively benign at low speed. Thus, the 3/rev flap bending moment is the key structural load at this low speed transition flight.

Figure 7 compares the flap bending moments between the high speed and high altitude stall flight. The 3/rev is again the dominant harmonic. In general the flap bending moments do not show the effect of stall. The effect of stall is seen in the torsion loads. Figure 8 compares the torsion loads between high speed and high altitude stall flights. As expected, the low frequencies (1-2/rev) are dominant at high speed. The higher frequencies are dominant in stall. The key mechanism behind torsion loads at high speed are the low frequency (1-2/rev) unsteady transonic pitching moments. The key mechanism at stall are the two cycles on the retreating side. The chord bending loads at the stall flight are not reliable.

ANALYSIS AND PREDICTION METHOD

The blade structural loads and, pitch link loads would be predicted using: (1) flight test measured airloads, damper force and control angles, and (2) first principles CFD/CSD loose coupling. The first step serves as a validation of the CSD model. In addition, it provides an approximate (due to unavoidable errors associated with test data measurements and interpolation) upper limit to the accuracy of loads prediction that can be obtained by using CFD.

The loose coupling method is same as the *delta* method originally proposed by Tung *et al* [16]. In recent years, the loose coupling method has been applied to obtain stable and converged Euler and Reynolds Averaged Navier-Stokes (RANS) solutions by several researchers [5, 6, 7, 8, 9, 11]. In the present study, the overset mesh based UMTURNS code (University of Maryland Transonic Unsteady Rotor Navier-Stokes, [15, 11]), is coupled with UMARC (University of Maryland Advanced Rotorcraft Code, [12]) comprehensive analysis. The comprehensive analysis provides the CSD model, trim model, and a basic aerodynamic model that provides airloads sensitivity to blade deformations necessary for trimming the rotor. In the present study a linear in-

flow and airfoil table look up based aerodynamics are used. The final converged airloads are entirely the CFD airloads, and are independent of the choice of this airload model.

UMARC Comprehensive Analysis CSD Model

The rotor blades are modeled as second-order non-linear, isotropic Euler-Bernoulli beams. The coupled flap-lag-torsion equations are based on Ref. [17]. The formulation is extended to include axial elongation and elastic twist as quasi-coordinates, based on Refs. [18] and [19]. The resultant almost-exact beam model is accurate up to moderate bending deflections of 15% radius (R) [20]. The rotor blade is treated as a fully articulated beam with flap and lag hinges coincident at 4.66% span. All blades are identical. Each blade is discretized into 20 finite elements undergoing flap, lag, torsion and axial degrees of motion. The blade property data, including nonlinear structural pre-twist and sweep are obtained from the NASA (Ames) master database. The non-linear lag damper force is imposed on the structure as a set of concentrated forces and moments acting at 7.6% of the blade span. The pitch link is modeled as a linear spring-damper system. The elastomeric bearing stiffness and damping are modeled as linear springs and dampers in flap, lag and torsion. The first eight structural modes are used for the present study. The rotor blade frequency plot and the first ten natural frequencies at the operating RPM are shown in Figure 9. These correspond to a collective angle of 14.5 degrees and a measured root torsion spring stiffness of 1090 ft-lb/degree [21]. The root spring stiffness is an equivalent measure of the pitch link stiffness.

UMTURNS with Wake Capture

The details of the CFD analysis used here can be found in Refs. [11] and [15]. To summarize, UMTURNS analysis is a Reynolds Averaged Navier-Stokes (RANS) code with overset mesh capability for wake capture. It includes the Spalart-Allmaras turbulence model [22], modified to account for near solid body rotation in vortex core regions. The blade deformations are incorporated using dynamically deforming meshes. The numerical scheme employs a modified finite volume method, second order accurate space and time. The flow field around each blade is calculated using a single block near body grid. The far field is resolved using a cylindrical background grid within which the four near body meshes are embedded. At every time step hole cutting and chimera interpolations are performed between the near blade and background grids. An overlap region of 2 chord distances is used.

The present calculations are performed with a relatively medium grid of 0.8 million points for the near blade mesh and 2.2 million points for the background mesh. The near blade grid has 133 points in the wrap around direction, 125 points in the spanwise direction and 48 points in the normal direction. An azimuthal step of 0.25 degrees is used. The computations are performed on four processor on a x86-64 cluster of speed 3.2 Gz. Each CFD iteration takes around 16 hours of wall clock time. A converged CFD/CSD solution can be obtained in approximately 6 to 8 UMARC/UMTURNS iterations.

CFD/CSD Coupling

The CFD airloads (normal forces, chord forces, and pitching moments at local quarter chord) are coupled at all radial stations from the root cut out to the tip. The airloads and blade deformations are transferred between CFD and comprehensive analysis at all spanwise grid points available in the respective codes. The comprehensive analysis accepts CFD airloads at 120 gauss points and provides blade deformations at the same points. Based on the CFD grid, the deformations are interpolated by the CFD analyses at 133 spanwise points.

The comprehensive analysis provides the CSD model, a lifting-line model, and the aircraft trim model. The CSD model is same as that described above, except that the measured lag damper force is not used. The lifting-line model provides the air load sensitivities to blade deflection. The lifting-line model is described in Ref. [6].

The trim model is a free flight propulsive trim for the entire aircraft. The three rotor control angles (collective, longitudinal and lateral cyclic angles), aircraft longitudinal and lateral tilts, and the tail rotor collective are calculated based on force and moment balance about the aircraft center of gravity. The fuselage aerodynamic properties are incorporated as functions of fuselage tilt. Fuselage dynamics is neglected. The aerodynamic properties are obtained from 1/4-scale wind tunnel experimental data (from Ames database). They include the effect of the horizontal tail. The zero-angle fuselage flat plate area is $36.34 ft^2$ [23]. The tail rotor properties and vertical tail cant angle are included. The main rotor has a three degree forward shaft tilt angle. The details of the propulsive trim analysis and validation are described in Ref. [12].

The coupling is performed using the following iterative steps.

1. A lifting-line comprehensive analysis solution is obtained. This provides the baseline blade deformations, trim angles, air loads.
2. Using the baseline solution, CFD air loads are calcu-

lated. These air loads are different from, and in general improved, compared to the baseline air loads.

3. The difference between the CFD air loads obtained in step 2 and lifting-line air loads are the *delta* air loads. The lifting-line analysis is now re-run with the delta air loads imposed in addition to the intrinsic lifting-line air loads. The delta air loads are held fixed over the trim iterations. The lifting-line air loads change from one trim iteration to another and provide the air load sensitivities required to trim the rotor. In addition, the lifting-line air loads provide aerodynamic damping which makes the loose coupling procedure well-posed and stable.
4. Step 2 and Step 3 is one CFD/CSD coupling iteration. The coupling iterations are performed until the delta air loads converge at every radial and azimuthal station.

The converged air loads are CFD air loads. They are equal to the converged lifting-line air loads plus the converged delta air loads. The converged delta airloads depend on the lifting-line analysis used, but the converged airloads are independent of the lifting-line solution.

FUNDAMENTAL UNDERSTANDING AND PREDICTION OF LOADS

The structural loads obtained at the three flight conditions are described below. The CFD/CSD loads are compared with those obtained from the standalone CSD model with flight test airloads imposed on the structure.

Low Speed Flight (C8513)

The predicted flap bending moments using measured airloads, and damper force are shown in figure 10. The effect of the damper force is limited to the inboard stations (11.3% R and 20% R) on the retreating side. Figure 11 shows predictions at 20% R with and without the measured damper force. In general, the effect of damper force is marginal. The flap bending moment predictions are accurate with measured airloads.

The first principles CFD/CSD predictions of flap bending moments are shown in figure 12. Even though the waveform and peak-to-peak is improved compared to a lifting-line model, significant discrepancy occurs in phase. The error lies in 3/rev prediction as shown in figure 13. Out of all the harmonics of the flap bending moment, the 3/rev component shows the largest discrepancy. The cause of discrepancy is not clear at present. The predicted lift is shown in figure 14. The two wake induced loadings in the first and fourth quadrants are well captured. The 3/rev magnitude and phase are in

well-predicted at stations, except at the inboard 50% of the blade where there is a significant over-prediction of the magnitude.

The chord bending moment predictions are shown in figures 15 and 16. Figure 15 shows predictions using measured airloads. The effect of the damper force is seen at stations occurring 40% R inboard and only on the lower harmonics, 1-3/rev. The predicted phase of all the harmonics are satisfactory. Discrepancies occur in the prediction of magnitude. All harmonics 2/rev and higher show an under-prediction, except the 5/rev, which shows a significant over-prediction. The measured chord forces are obtained by pressure integration and do not incorporate the viscous drag. However, this does not appear to be the source of the discrepancy. Figure 15 compares CFD/CSD predictions with those obtained using measured airloads. Predictions are compared consistently without using the measured damper force. The CFD/CSD predictions contain the entire chord force. The key discrepancy in predictions remain. The 3 and 4/rev are under-predicted, the 5/rev is over-predicted.

The torsion loads are shown in figures 17 and 18. Figure 17 shows predictions using measured airloads. The sharp drop in the fourth quadrant is not captured even with measured airloads. The damper force improves prediction in the fourth quadrant but the effect is seen only on the pitch link load. The peak torsion moments at the outboard stations 70% R and 90% R remain uncaptured. The trends are similar using CFD/CSD, as shown in figure 18.

High speed flight (C8534)

The most significant contribution of CFD lies in high speed flight: the accurate prediction of three dimensional unsteady transonic pitching moments at the outboard stations (86.5% R outboard for the UH-60A). This is a fundamental improvement, analysed in Refs. [3] and [4] using isolated airloads and structural loads calculations, and then in Refs. [5] and [6, 11] using fully coupled CFD/CSD calculations.

Figure 19, from Ref. [11], shows the key CFD/CSD airloads predicted at this flight condition. Accurate pitching moment predictions generate accurate elastic twist. Accurate elastic twist generates accurate vibratory lift harmonics, which in turn contributes significantly to the accuracy of the advancing blade lift waveform [6]. Elastic twist is the key contributor at the outboard stations (96.5% R). Elastic twist alone is not enough inboard (77.5% R). Wake interactions caused by positive vorticity moving inboard in the regions of negative lift create the secondary lift impulse at the junction of the first and second quadrant [4]. Figure 20 shows the predicted flap bending moments. Predictions are

compared from CFD/CSD calculations and from measured airloads. There is an unresolved phase difference of around 7 degrees between the two predictions, and an additional 7 degrees between predictions from measured airloads and flight test. The predictions from measured airloads serve as an upper limit to the improvement that can be obtained by refining the aerodynamic calculations. Figure 21 compares the magnitude and phase of the first five harmonics. Predictions are similar to that using measured airloads except for the under-prediction of 5/rev. The azimuthal phase error of around 7 degrees, shown in figure 20 appears as a constant shift in the phase of the first three harmonics. The torsion loads are shown in figure 22. The large oscillation between the first and second quadrant, caused by the transonic pitching moment variations, define the peak to peak loading. It is accurately captured. In general the lower harmonics, 1-3/rev are well predicted. Discrepancies occur at the higher harmonics, 4/rev and higher. This discrepancy appears as a prediction error in the fourth quadrant. The error appears to stem from inaccuracies in structural dynamic modeling. As shown in figure 22, the error is not resolved even using measured airloads. The damper force appears to improve the waveform on the retreating side, but it does not fully resolve the higher harmonics. Unmodeled dynamics of the hub and the swashplate and the kinematics of the concentrated damper force and pitch link assembly may have a bearing on the problem and are currently under investigation. Note that even though the peak to peak pitch link load are determined by the lower frequencies, the higher frequencies (3/rev and higher for a four bladed rotor) determine the peak to peak variation of the servo actuator loads below the swashplate in the fixed frame. The higher harmonic errors are seen in the radial distribution of torsion moments in figure 23. In general the CFD/CSD predictions are close to those obtained using measured airloads, except the 3/rev harmonic where CFD/CSD show a significant under-prediction. Both sets of predictions in figure 23 have been obtained without using the damper force. Thus the differences arise entirely out of the airloads. The chord bending moments are compared in figures 24 and 25. Figure 24 shows the predicted chord bending moment harmonics with and without the damper force. The trends are similar as those obtained earlier in the case of low speed flight. The damper force appears to mainly effect the lower frequencies at radial stations 40% R inboard. The phase predictions are satisfactory. The 4/rev shows a significant under-prediction while the 5/rev shows a significant under-prediction. The damper force does not affect this higher harmonic prediction. The measured airloads, as mentioned earlier, are obtained using integrated pressure loads and do not incorporate the viscous drag component. Predictions us-

ing CFD/CSD, as in figure 25, show the effect of viscous drag. Viscous drag does not appear to be the source of the 4 and 5/rev prediction problem. The CFD/CSD predictions are marginally improved for the 3/rev harmonic at the outboard stations. In general they are close. The under-prediction of 4/rev and over-prediction of 5/rev remain.

High Altitude Dynamic Stall Flight (C9017)

The predicted lift (1-10/rev) at 86.5% R is shown in figure 26. The retreating blade stall is predicted by both the turbulence models. The first lift stall occurs around 250 degrees, the second lift stall around 320 degrees azimuth. The waveform in the first quadrant, and the pre-stall trough in the third quadrant are not satisfactorily captured. This leads to a large error in the phase of 3/rev flap bending moments. The flap bending moment at 70% R is shown in figure 27. The peak loading in the fourth quadrant is captured. However significant errors exist in the waveform. The error stems from the predicted airloads. Predictions using measured airloads show the correct trends. (figure 28). The predicted quarter-chord pitching moments are shown in figure 29. There is no phenomenological difference in stall prediction from the two turbulence model. The first pitching moment stall occurs around 230 degrees, the second stall around 300 degrees. The cycles were studied in Ref. [10] and shown to be associated with trim and elastic twist deformations. The first stall is a trim stall. It occurs due to the general rise in the sectional angle of attack caused by high trim angles. The strength and location of the second stall is related to an elastic twist peak occurring in the fourth quadrant. The peak is generated by 4 and 5/rev elastic twist deformations. Thus the mechanism appears to be as follows: the high trim angles create the first stall, this stall then triggers 4 and 5/rev elastic twist deformations which affects the second stall. The first torsion frequency of the rotor is 4.3/rev. In addition to elastic twist, the second stall is also sensitive to inflow distribution. The shaft tilt angle at this flight condition is negligible, around -0.15 degrees. Thus, the inflow is primarily induced in nature.

The physics behind the stall loads is studied by tracing the stall vortices over the blade chord. The stall vortices produce pressure pulses as they sweep over the blade chord. These pulses are identified in figure 30. It shows the azimuthal pressure variation at 18 chord-wise locations in an offset format. Negative pressure is plotted, therefore a higher value signifies a higher suction at a chord location. Note that the curves are arbitrarily offset from one another for better understanding of the flow physics. The focus here is on understanding the flow phenomena rather than the exact pressure values.

The curve at the top is the pressure plot for the leading edge, the curve at the bottom is the pressure plot for the trailing edge.

The suction effect of the dynamic stall vortex is visible from 0.36 chords to the trailing edge. Its movement over the chord is reflected in the finite lag in azimuth from one chord station to the next. Its passage over the trailing edge signifies lift stall. This azimuth is easily identified. Its formation and detachment from the leading edge signifies moment stall. This azimuth is not visible, because of the generally high pressure levels below 0.36c. Conceptually, for a rough estimate, the dotted line tracing the vortex can be extrapolated upward. Similarly, the dotted line showing the regions of near supercritical flow, at the leading edge, can be extrapolated downward. The two lines intersect near 0.08c. The stall vortex may co-exist in a locally sonic flow regime near this chord station. There is a second suction peak in the fourth quadrant. Near the leading edge, up to 0.12c, it remains at the same azimuth. This is caused by the elastic twist oscillation in the fourth quadrant. Whether this peak triggers a second stall vortex is not very clear. However this pressure peak appears to gain an azimuthal movement, downstream of 0.12c, producing a stall like perturbation. The pressure curves in the advancing side show a shock. It appears to be formed near 0.2c and moves forward towards 0.12c with increase in azimuth and incident Mach number. The shock appears to induce pressure perturbations in the second quadrant which explains the higher harmonic pitching moment waveform in the second quadrant.

The stall azimuths extracted from the airload plots can be used to generate a stall map over the disk. The test data used for comparison has been obtained from Ref. [14] and shifted in azimuth by 14 degrees. The trends are similar in the two stall regions. There are discrepancies in the test data which are not clearly understood at present. For example, the test data for the second lift stall shows a significant lag in azimuthal onset, whereas figure 26 shows no such discrepancy. The first lift stall shows a lead in azimuthal onset which is also not consistent with figure 26. The moment stall patterns are consistent. The first stall appears at 55% R around 230 degree azimuth, moves forward in azimuth and shifts back again. The second moment stall occurs over a smaller region near the outboard stations. It appears more 2D in nature without a distinct radial pattern. As mentioned before, the first stall appears to be due to trim angles generating high sectional angles of attack. Note that the control angles for the high speed case are higher than this flight condition. However the shaft is tilted forward by 7 degrees in high speed. Here the shaft tilt is only -0.15 degrees. Thus the stall occurs over a larger spanwise extent. The second stall location is af-

ected largely by elastic twist perturbation in the fourth quadrant. Whether it is triggered depends on the local inflow. This is a possible reason behind why, even though the twist excitation remains similar in magnitude from 50% R outboard, the stall occurs over a lesser spanwise extent.

The torsion loads are shown in figure 32. The peak to peak values are correct. As before, the discrepancies are in higher harmonics of torsion loads. The radial distribution of torsion moments is shown in figure 33. The magnitude and phase of the first five harmonics are compared between CFD/CSD and measured airloads. Predictions from both the turbulence models are compared. The trends are similar up to the first three harmonics. Differences exist in the 4 and 5/rev stall loads. The high frequency errors are reflected in the pitch link loads. The pitch link load predictions are summarized in figure 34. Predictions at all three flights are compared using both CFD and measured airloads. The high speed and stall flights show the highest peak to peak variation due to a high 1/rev content. The low speed load is relatively benign as discussed earlier. The trends in vibratory harmonics are not well predicted either at high speed or stall. The stall flight shows a high 6/rev content. This trend is also not captured.

Conclusions

The UH-60A main rotor structural loads were studied at three critical level flight conditions. Predictions using CFD/CSD loose coupling were compared with flight test data and with predictions using measured airloads, damper force and control angles. Based on this study the following conclusions are made.

1. The peak-to-peak flap bending moments, torsion moments and pitch link loads are accurately captured at all flight conditions. This is because the low frequencies (1-3/rev) are well predicted in magnitude. The peak-to-peak chord bending moments are under-predicted because of under-prediction of 1 and 2/rev.
2. The predicted vibratory flap bending moments are satisfactory at high speed, less satisfactory at stall, and unsatisfactory at low speed. The 3/rev is the dominant vibratory harmonic in all three flight conditions. The 3/rev is under-predicted by 15% at high speed. This discrepancy remains even with measured airloads. The 4/rev is well predicted. The 5/rev is severely under-predicted. This appears to be an aerodynamic problem because it is resolved using measured airloads. At low speed, the 3/rev is under-predicted by about 70%. The discrepancy

is removed using measured airloads. The CFD predicted 3/rev lift distribution does not show a similar error in magnitude, even though stations inboard of 50% R show a large under-prediction. The cause of the 3/rev flap bending moment error is not clear at present. The 4/rev prediction is poor at stations 50% R inboard. The 5/rev is well predicted. At stall, the magnitude of 3/rev is well captured but there is a significant error in phase. The problem is again aerodynamic in nature because accurate predictions are obtained using measured airloads.

3. The predicted vibratory chord bending moments show large errors in the magnitude of 4 and 5/rev. The phase predictions are satisfactory. The 4/rev is over-predicted, and the 5/rev under-predicted. This discrepancy occurs consistently at all the three flights. The problem remains with measured airloads. CFD/CSD predictions are similar to predictions using measured airloads. Therefore, the absence of viscous drag in the measured airloads does not appear to be the source of the problem. The damper force at the root affects predictions at stations 40% R inboard, and only for the 1-3/rev harmonics.
4. The predicted torsion moments show discrepancies in the 4 and 5/rev harmonics. Like in the case of chord bending moments, this discrepancy is not resolved using measured airloads. The problem therefore appears to be structural dynamic in origin. The integrated effect of this deficiency appears in the 4 and 5/rev pitch link loads. In general, none of the vibratory harmonics (3,4 or 5/rev) of the pitch link load are accurately predicted.

REFERENCES

- [1] William G. Bousman, "Putting the Aero Back Into Aeroelasticity," 8th Annual ARO Workshop on Aeroelasticity of Rotorcraft Systems, University Park, PA, October, 1999.
- [2] Bousman, W. G., "A Qualitative Examination of Dynamic Stall from Flight Test Data," American Helicopter Society 53rd Annual Forum, Virginia Beach, VA, April 1997.
- [3] Sitaraman, J., Baeder, J. D., and Chopra, I., "Validation of UH-60 Rotor Blade Aerodynamic Characteristics using CFD," 59th Annual Forum of the American Helicopter Society, Phoenix, AZ, May 6-8, 2003.
- [4] Datta, A., and Chopra, I., "Validation of Structural and Aerodynamic Modeling Using UH-60A

- Airloads Program Data,” *Journal of the American Helicopter Society*, Vol. 50, No. 1, January 2006, pp 43-58.
- [5] Potsdam, M., Yeo, Hyeonsoo, Johnson, Wayne, “Rotor Airloads Prediction Using Loose Aerodynamic/Structural Coupling,” Presented at the American Helicopter Society 60th Annual Forum, Baltimore, MD, June 7-10, 2004.
- [6] Datta, A., Sitaraman, J., Chopra, I, and Baeder, J., “CFD/CSD Predictions of rotor vibratory loads in high-speed flight,” in press for publication in the *Journal of Aircraft*. Revised version of “Analysis Refinements for Prediction of Rotor Vibratory Loads in High-Speed Forward Flight,” American Helicopter Society 60th Annual Forum, Baltimore, MD, June 7-10, 2004.
- [7] Altmikus, A. R. M., Wagner, S., Beaumier, P., and Servera, G., “A Comparison : Weak versus Strong Modular Coupling for Trimmed Aeroelastic Rotor Simulation,” American Helicopter Society 58th Annual Forum, Montreal, Quebec, June 2002.
- [8] Pahlke, K. and Van Der Wall, B., “Progress in Weak Fluid-Structure-Coupling for Multibladed Rotors in High-Speed Forward Flight,” 28th European Rotorcraft Forum, September 17-20, Bristol, U.K., 2002.
- [9] Pomin, H. and Wagner, S. “Aeroelastic Analysis of Helicopter Rotor Blades on Deformable Chimera Grids,” *Journal of Aircraft*, Vol. 41, No. 3, May-June 2004.
- [10] Datta, A., Chopra, I., “Prediction of UH-60A Dynamic Stall Loads in High Altitude Level Flight using CFD/CSD Coupling,” 61st Annual Forum of the American Helicopter Society, Grapevine, Texas, June 1-3, 2005.
- [11] Sitaraman, J., Datta, A., Baeder, J., and Chopra, I., “Prediction of Rotor aerodynamic and structural loads at three critical level flight conditions,” 31st European Rotorcraft Forum, Florence, Italy, Sep. 12-15, 2005.
- [12] Datta, A., Chopra, I., “Validation and Understanding of UH-60A Vibratory Loads in Steady Level Flight,” *Journal of the American Helicopter Society*, Vol. 49, No. 3, July 2004, pp 271-287.
- [13] Crews, S. T., “Rotorcraft Vibration Criteria, A New Perspective,” American Helicopter Society 43rd Annual Forum, St. Louis, MO, May 1987.
- [14] Kufeld, R., M., Bousman, W., G., “High Load Conditions Measured on a UH-60A in Maneuvering Flight,” American Helicopter Society 51th Annual Forum, Forth Worth, TX, May 1995.
- [15] Duraisamy, K., Sitaraman, J., and Baeder, J., “High Resolution Wake Capturing Methodology for Improved Rotor Aerodynamic Computation,” American Helicopter Society 61st Annual Forum, Texas, June 7-10, 2005.
- [16] Tung, C., Caradonna, F., X. and Johnson, W., “Conservative Full Potential Model for Unsteady Transonic Rotor Flows,” *AIAA Journal*, Vol. 25, No. 2, 1987 p 193-198.
- [17] Hodges, D. H., and Dowell, E. H., “Nonlinear Equations of Motion for the Elastic Bending and Torsion of Twisted Nonuniform Rotor Blades”, NASA TN D-7818
- [18] Ormiston, R. A., Hodges, D. H., and Peters, D. A., “On the Nonlinear Deformation Geometry of Euler-Bernoulli Beams, NASA Technical Paper 1566.
- [19] Kvaternik, Raymond G., Kaza, Krishna R. V., Nonlinear Curvature Expressions for Combined Flapwise Bending, Chordwise Bending, Torsion, and Extension of Twisted Rotor Blades, NASA TM X-73, 997, 1976.
- [20] Johnson, W., “Rotorcraft Dynamics Models for a Comprehensive Analysis,” 54th Annual Forum of the American Helicopter Society, Washington D.C., May 20-22, 1998.
- [21] Kufeld, R. M., Johnson, W. “The Effects of Control System Stiffness Models on the Dynamic Stall Behavior of a Helicopter”, American Helicopter Society 54nd Annual Forum Proceedings, Washington, D.C., May 20-22.
- [22] Spalart, P. R. and Allmaras, S. R., “A One-equation Turbulence Model for Aerodynamic Flows,” AIAA Paper 92-0439, 1992.
- [23] Yeo, H., Bousman, W. G., Johnson, W., “Performance Analysis of a Utility Helicopter with Standard and Advanced Rotors”, AHS International Technical Specialists Meeting on Aerodynamics, Acoustics, and Test and Evaluation, San Francisco, January 23-25, 2002.

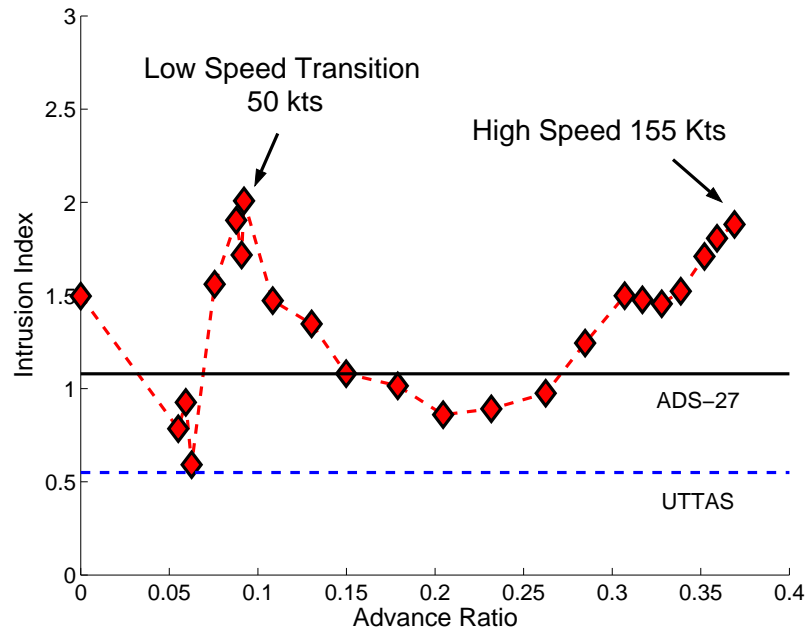


Figure 1: Measured Vibration at Pilot Seat of the UH-60A in Steady Level Flight, for take off weight 16,500 lbs, Ref.[1]

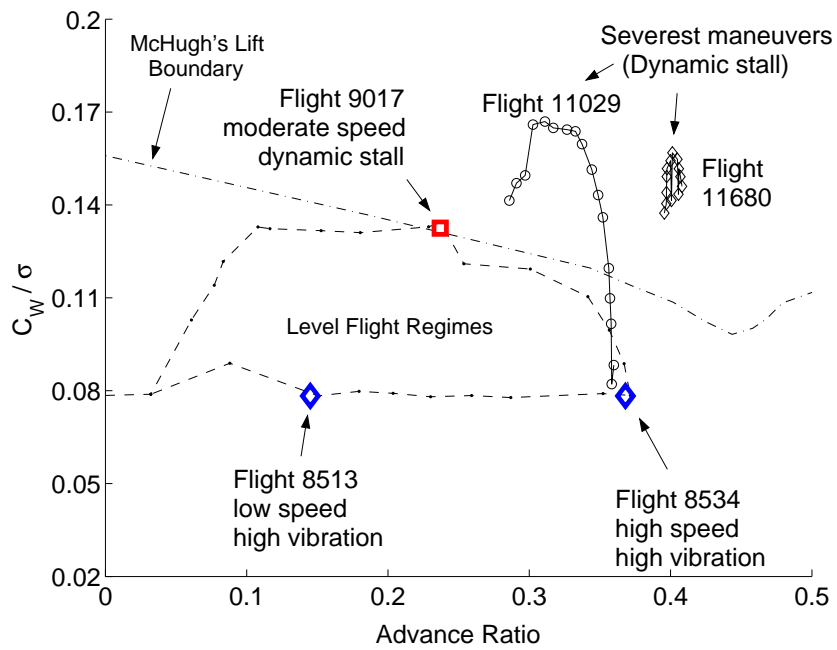


Figure 2: Weight-speed envelop of the UH-60A showing the two severest maneuvers, and the three critical level flight conditions

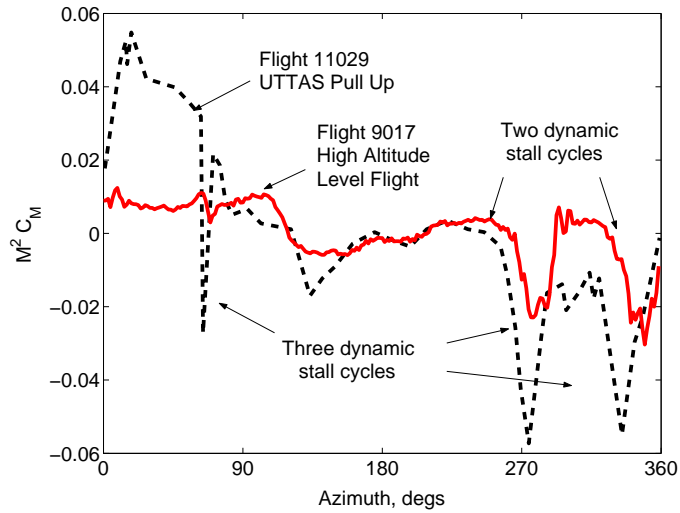


Figure 3: Retreating blade stall cycles of a high altitude level flight (Flight 9017) are qualitatively similar to a pull up maneuver (Revolution 14 of Flight 11029)

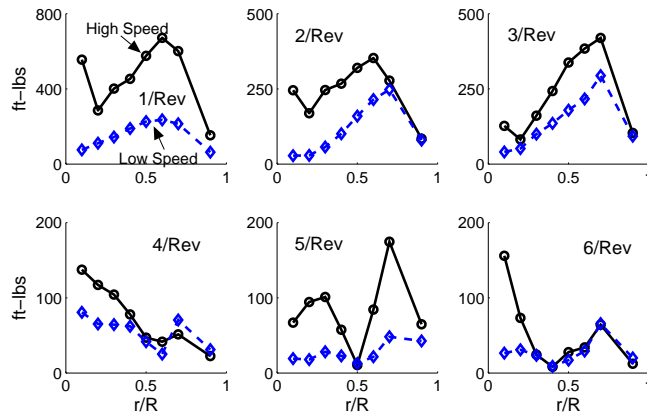


Figure 4: Measured flap bending moments at high and low speed flights (C8534 and C8513)

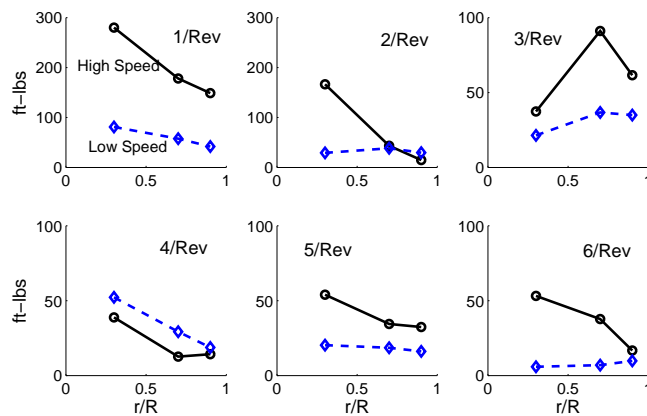


Figure 5: Measured torsion moments at high and low speed flights (C8534 and C8513)

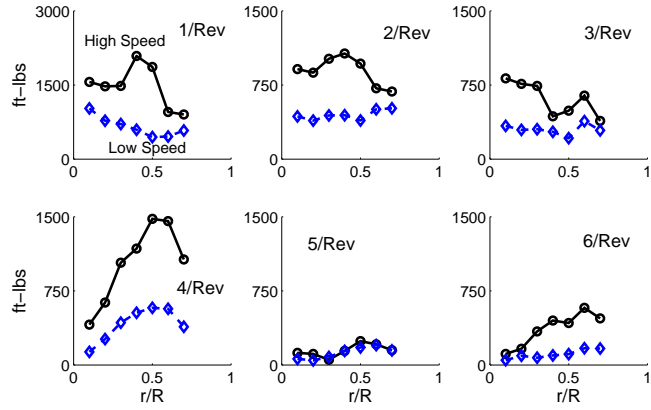


Figure 6: Measured chord bending moments at high and low speed flights (C8534 and C8513)

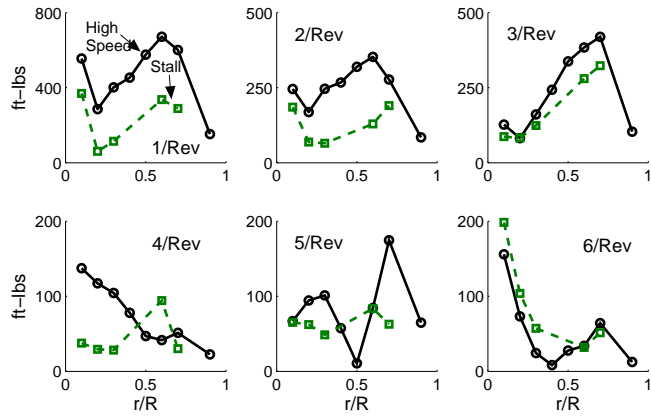


Figure 7: Measured flap bending moments at high speed and high altitude stall flights (C8534 and C9017)

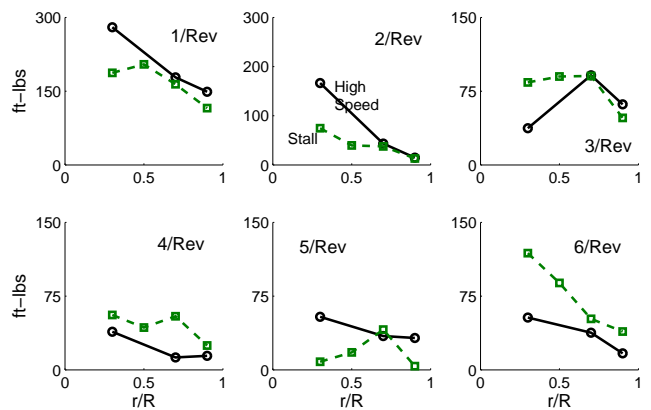


Figure 8: Measured torsion moments at high speed and high altitude stall flights (C8534 and C9017)

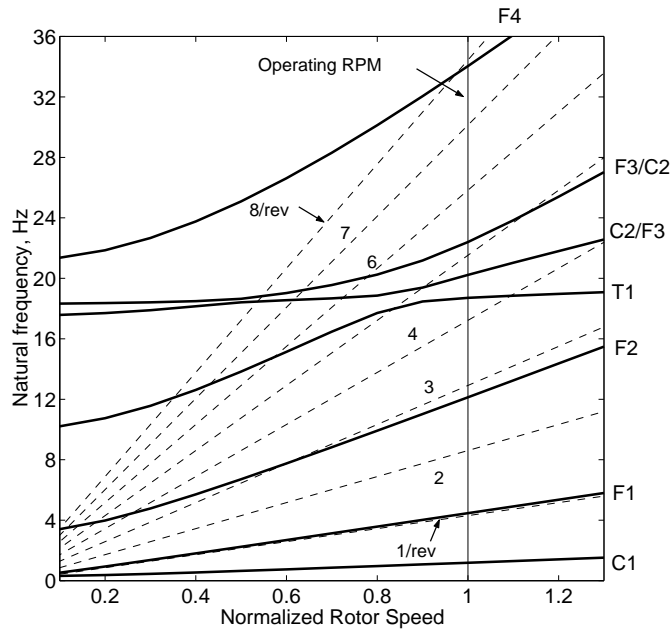


Figure 9: UH-60A rotor blade frequencies; Collective Angle 14.5 degrees; Effective root spring stiffness 1090 ft-lbs/degree; F:Flap, C:Chord-wise, T:Torsion; Operating frequencies: 0.28, 1.04, 2.82, 4.3, 4.7, 5.2, 7.9, 11.3, 12.4 and 12.6/rev

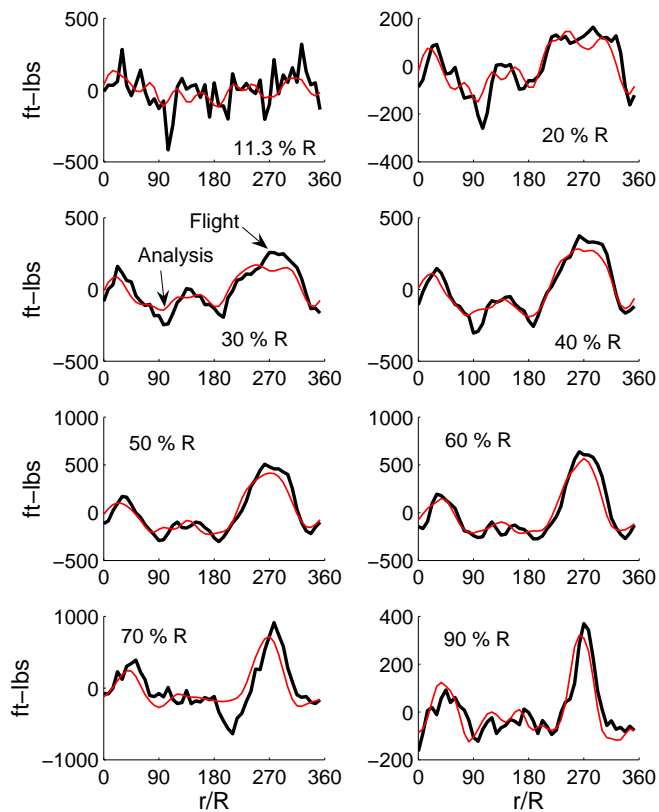


Figure 10: Measured and predicted flap bending moments for low speed flight C8513; Predictions using measured airloads

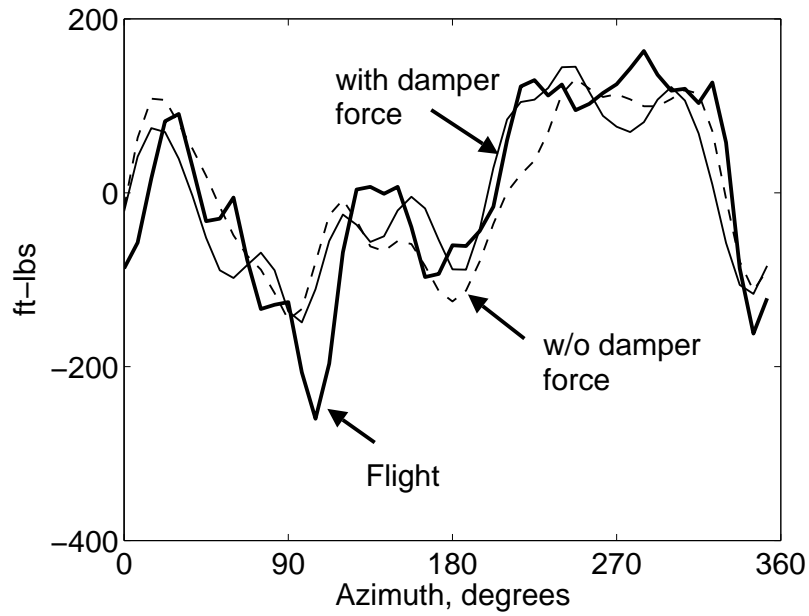


Figure 11: Measured and predicted flap bending moments for low speed flight C8513 at 20% R using measured airloads, with and without the measured damper force

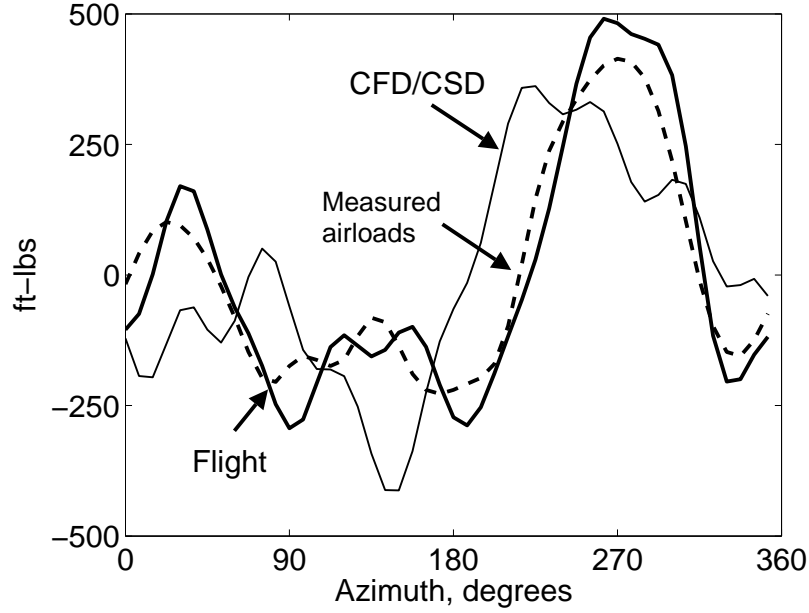


Figure 12: Measured and predicted flap bending moments for low speed flight C8513 at 50% R; Predictions using lifting-line and CFD

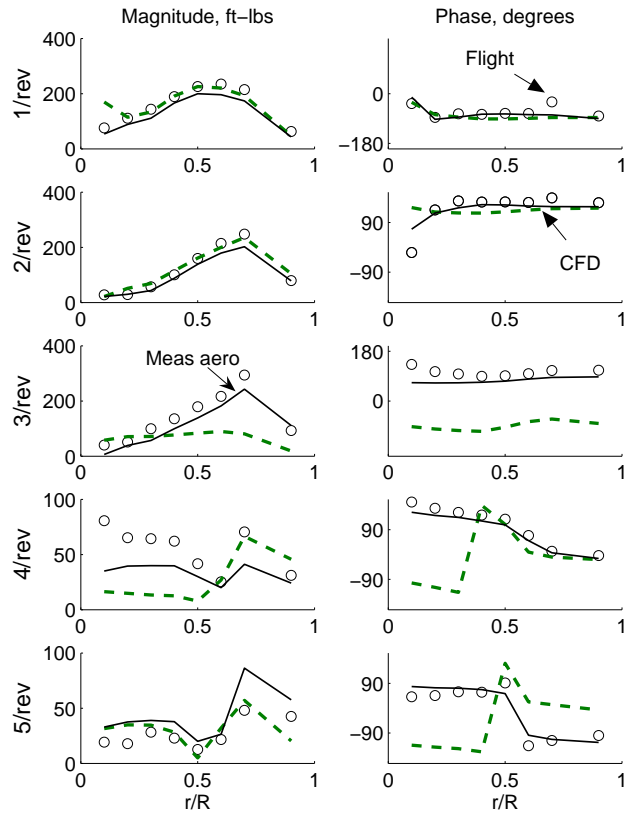


Figure 13: Measured and predicted flap bending moment harmonics at low speed flight C8513; Predictions using CFD/CSD compared with measured airloads

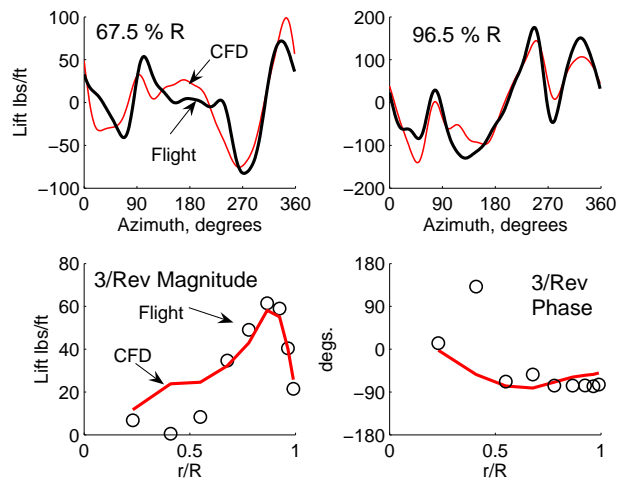


Figure 14: Measured and predicted lift (1-10/rev) at two radial stations, and distribution of 3/rev lift (magnitude and phase) over the blade span; Low speed flight C8513; Predictions using CFD/CSD

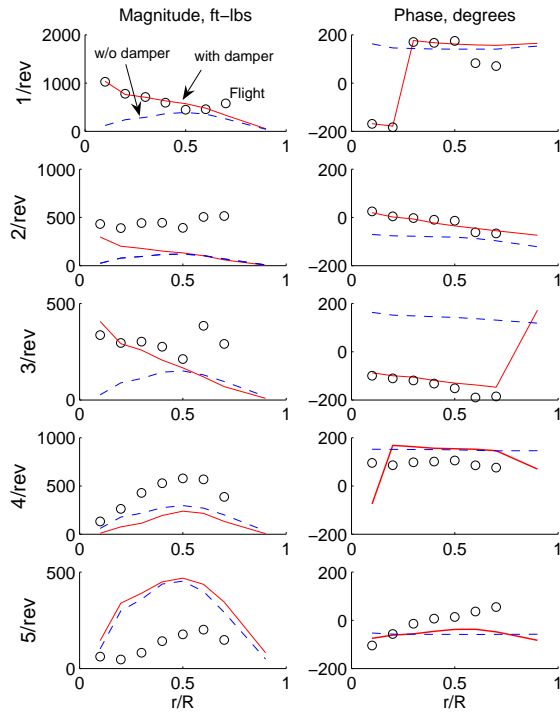


Figure 15: Measured and predicted chord bending moment harmonics at low speed flight C8513; Predictions using measured airloads compared with and without measured damper force

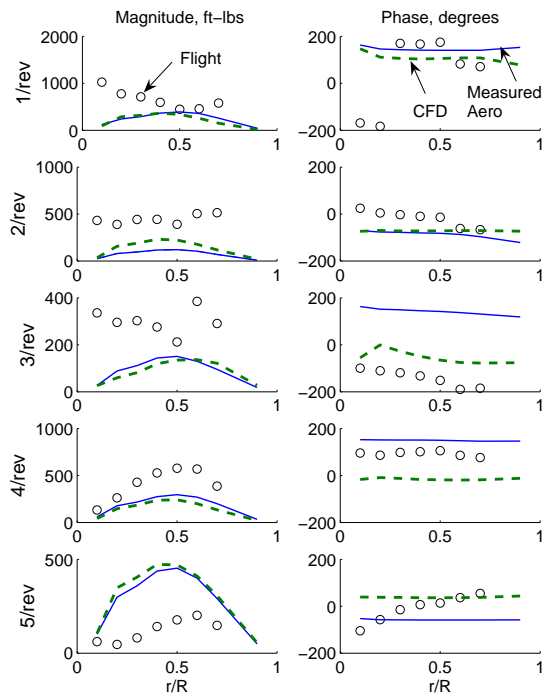


Figure 16: Measured and predicted chord bending moment harmonics at low speed flight C8513; Predictions using CFD/CSD compared with measured airloads

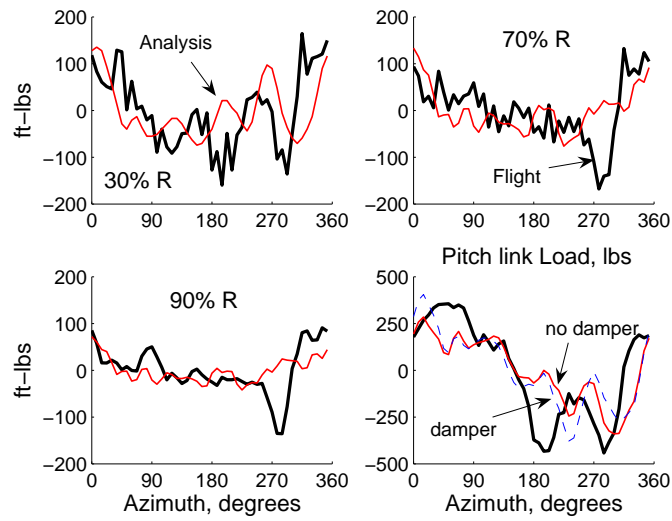


Figure 17: Measured and predicted torsion moments and pitch link load for low speed flight C8513; Predictions using measured airloads

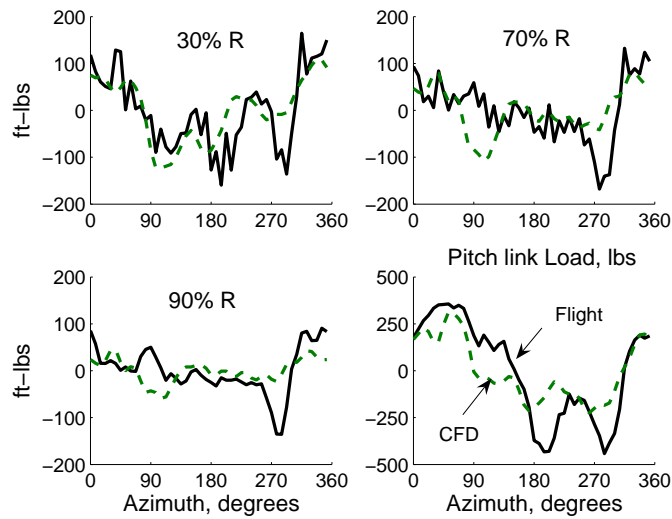


Figure 18: Measured and predicted torsion moments and pitch link load for low speed flight C8513; Predictions using CFD/CSD

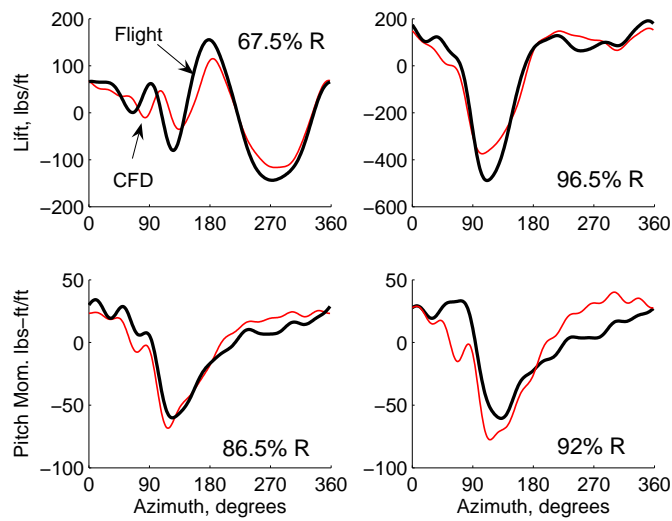


Figure 19: Measured and predicted lift and quarter-chord pitching moments (1-10/rev) at high speed flight C8534; Predictions using CFD/CSD

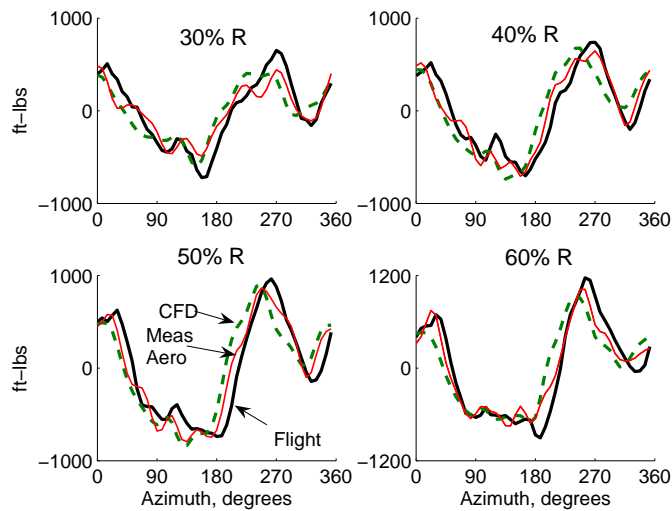


Figure 20: Measured and predicted flap bending moments (1-10/rev) at high speed flight C8534; Predictions using CFD/CSD

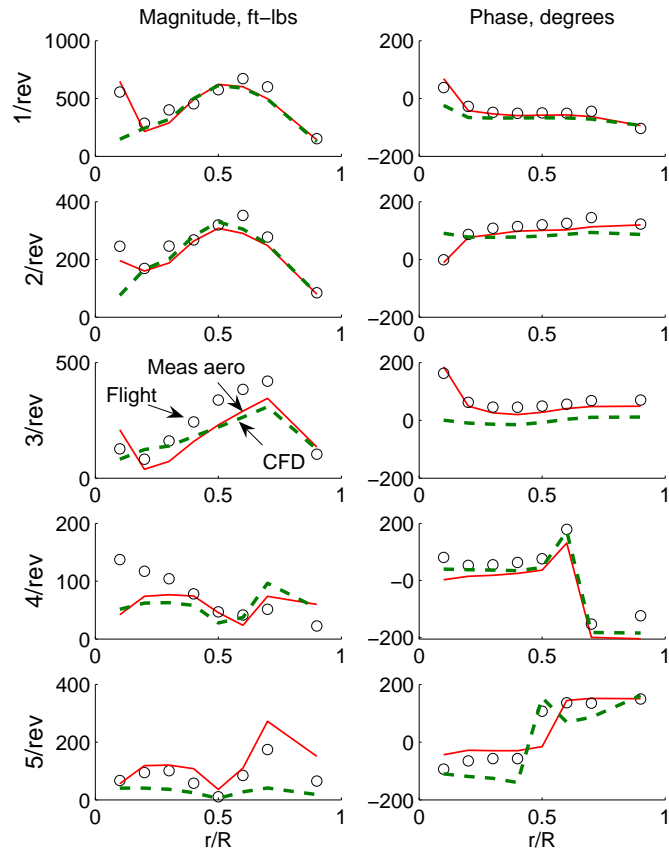


Figure 21: Measured and predicted flap bending moment harmonics (1-5/rev) at high speed flight C8534; Predictions using CFD/CSD compared with predictions using measured airloads

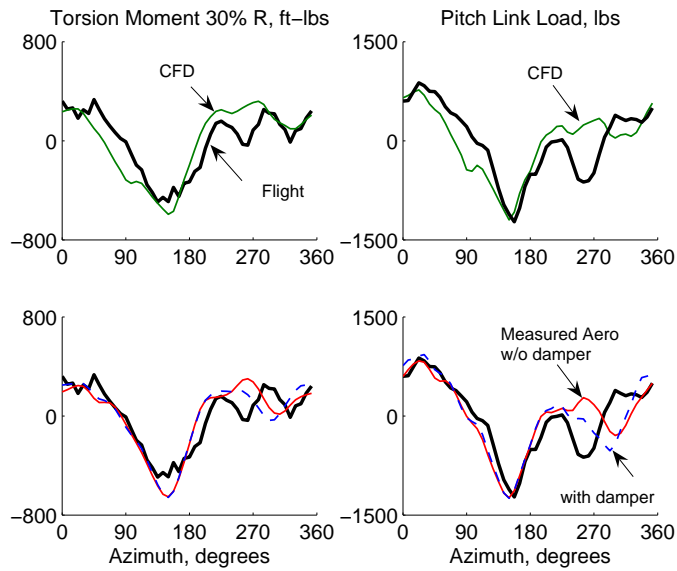


Figure 22: Measured and predicted torsion moments (1-10/rev) at high speed flight C8534; Predictions using CFD/CSD compared with predictions using airloads measured in flight

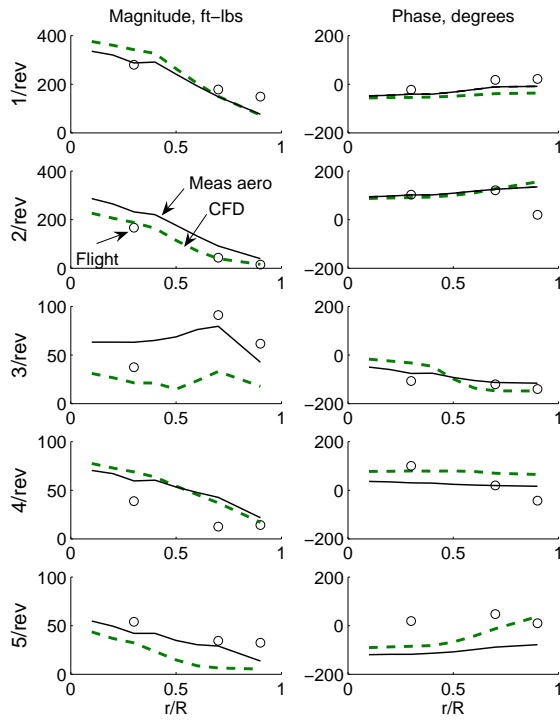


Figure 23: Measured and predicted torsion moment harmonics (1-5/rev) at high speed flight C8534; Predictions using CFD/CSD compared with predictions using measured airloads

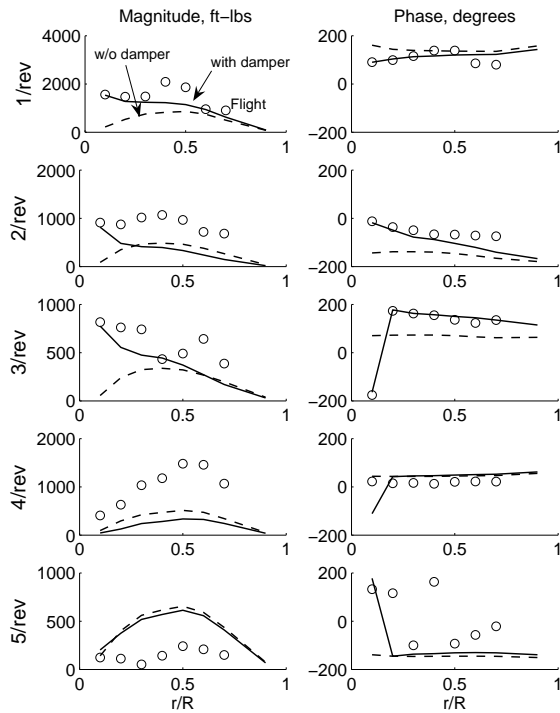


Figure 24: Measured and predicted chord bending moments (1-10/rev) at high speed flight C8534; Predictions using measured airloads compared with and without the measured damper force

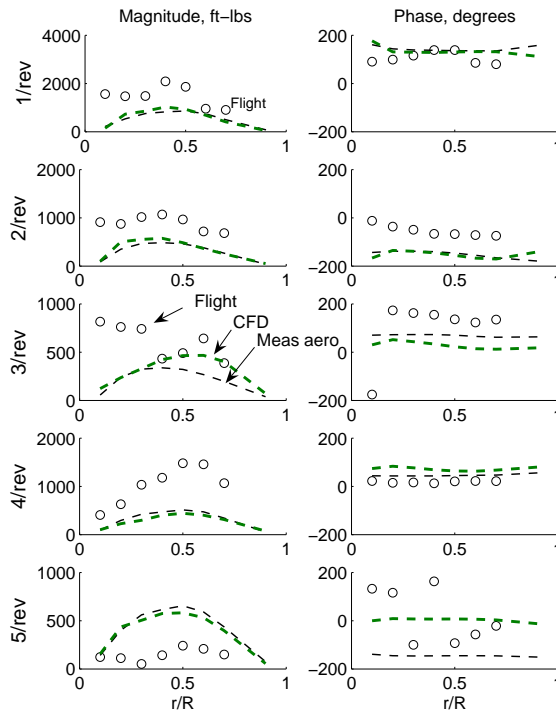


Figure 25: Measured and predicted chord bending moment harmonics (1-5/rev) at high speed flight C8534; Predictions using CFD/CSD compared with predictions using airloads measured in flight

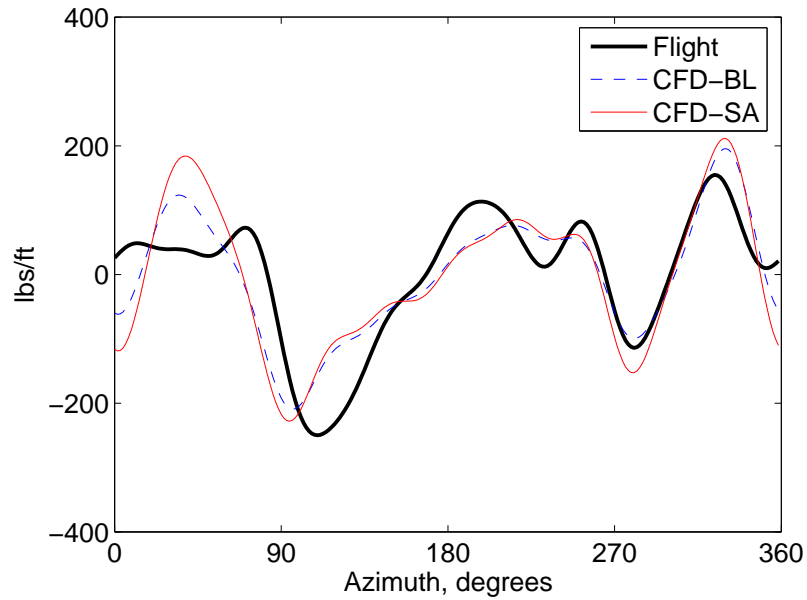


Figure 26: Measured and predicted lift (1-10/rev) at 86.5% R in the high altitude dynamic stall flight C9017

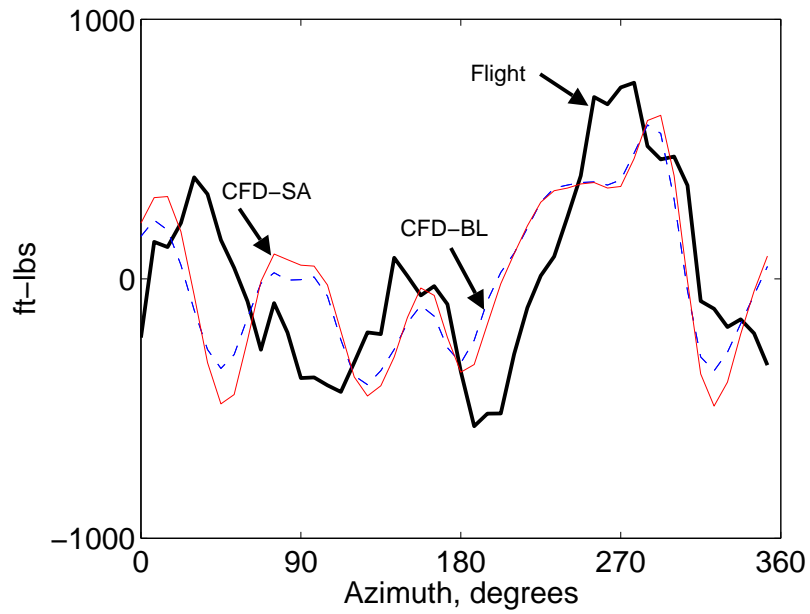


Figure 27: Measured and predicted flap bending moment (1-10/rev) at 70% R in the high altitude dynamic stall flight C9017

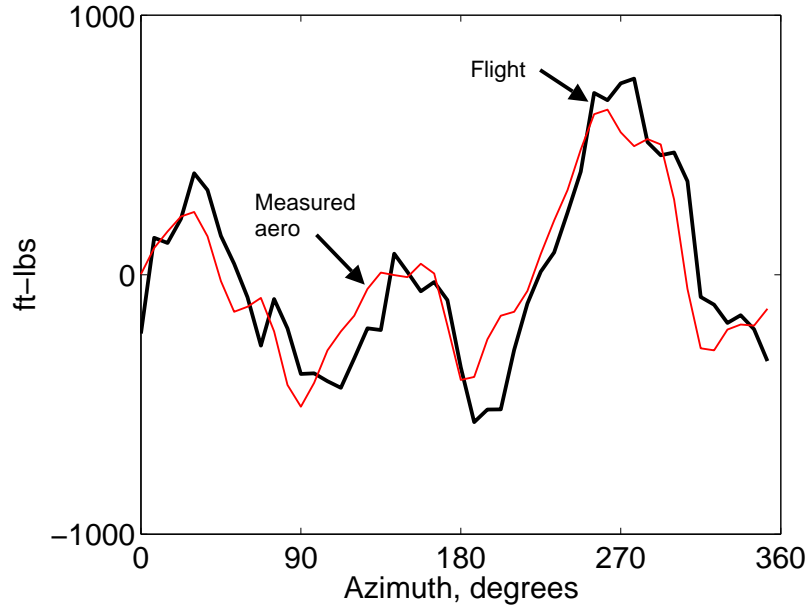


Figure 28: Measured and predicted flap bending moment (1-10/rev) at 70% R in the high altitude dynamic stall flight C9017; Predictions using airloads measured in flight

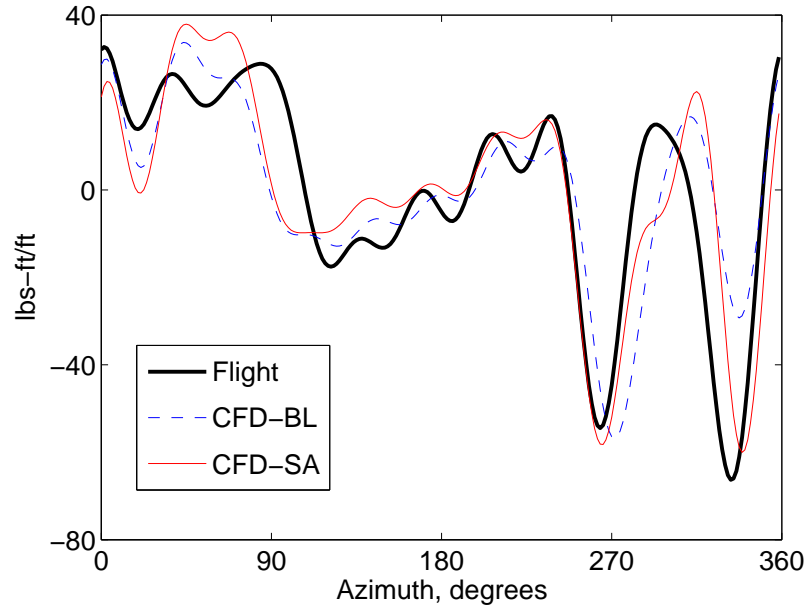


Figure 29: Measured and predicted quarter-chord pitching moment (1-10/rev) at 86.5% R in the high altitude dynamic stall flight C9017

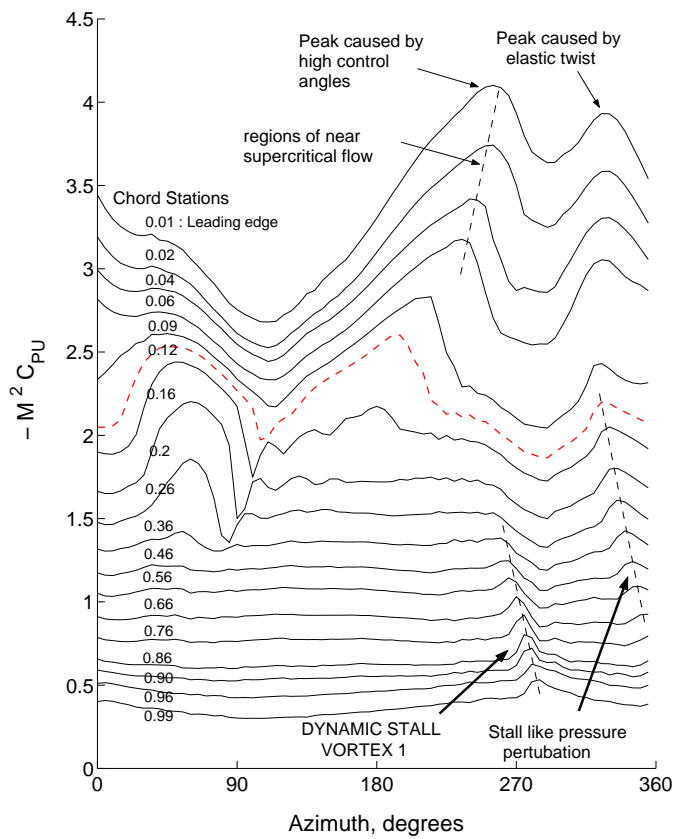


Figure 30: Azimuthal variation of upper surface chord-wise pressure at 86.5% R showing the movement of dynamic stall vortex; CFD/CSD predictions for flight C9017

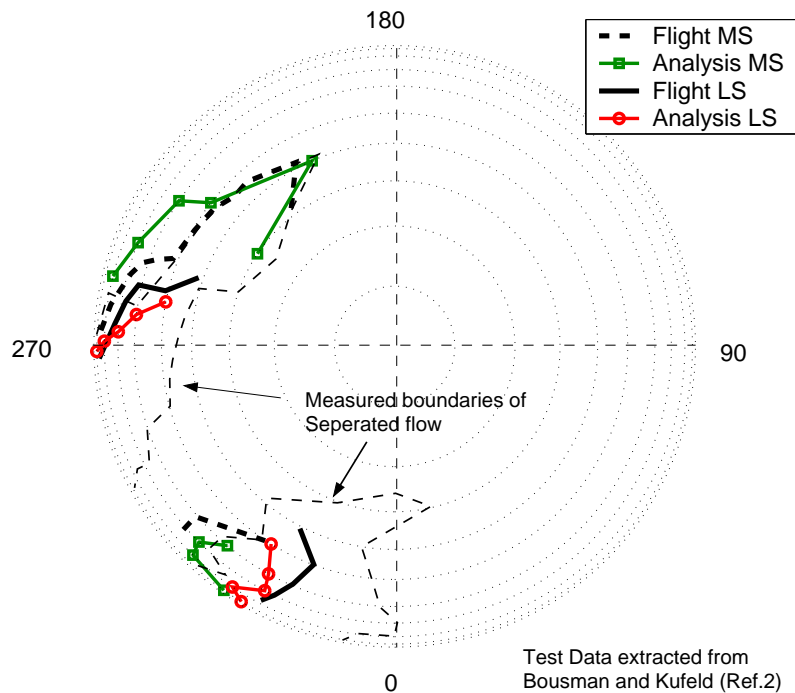


Figure 31: Azimuthal variation of lift and pitching moment stall; measured estimates compared with CFD/CSD coupled predictions; Flight C9017

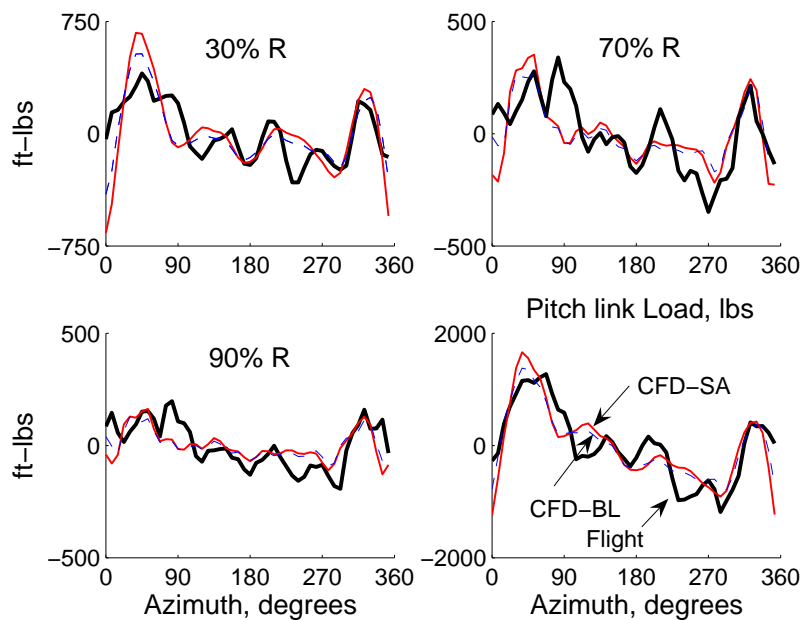


Figure 32: Measured and predicted torsion moments (1-10/rev) at the high altitude dynamic stall flight C9017; Predictions using CFD/CSD

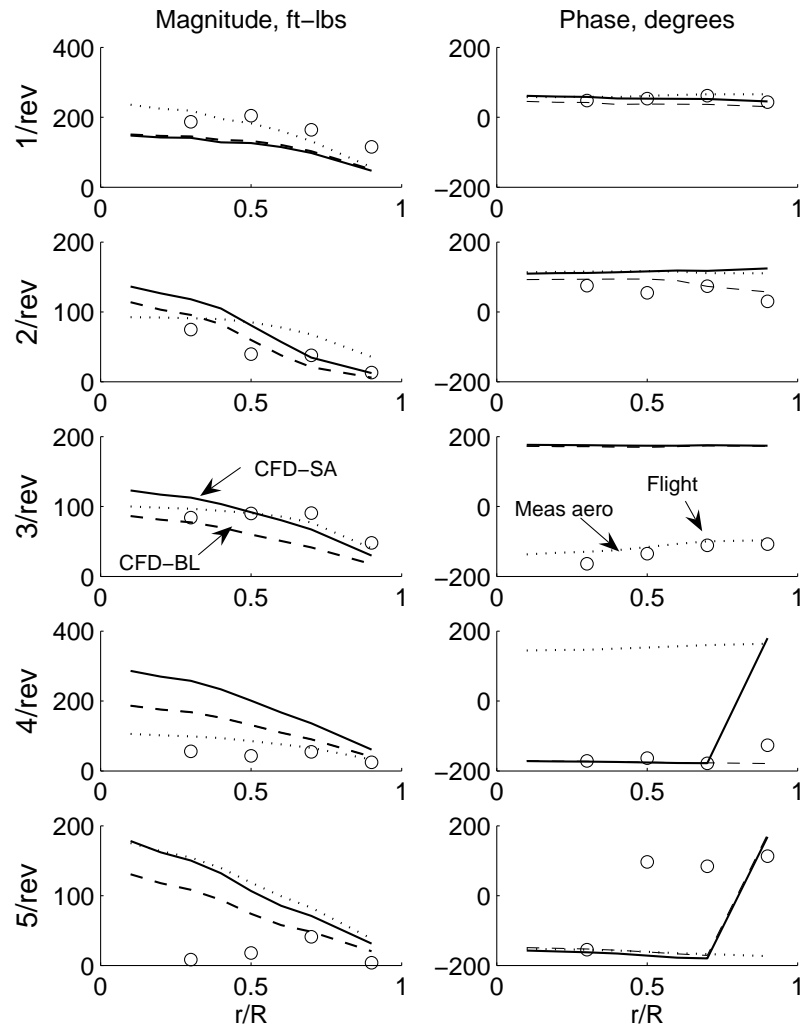


Figure 33: Measured and predicted torsion moments harmonics (1-5/rev) at the high altitude dynamic stall flight C9017; Predictions using CFD/CSD compared with predictions using measured airloads

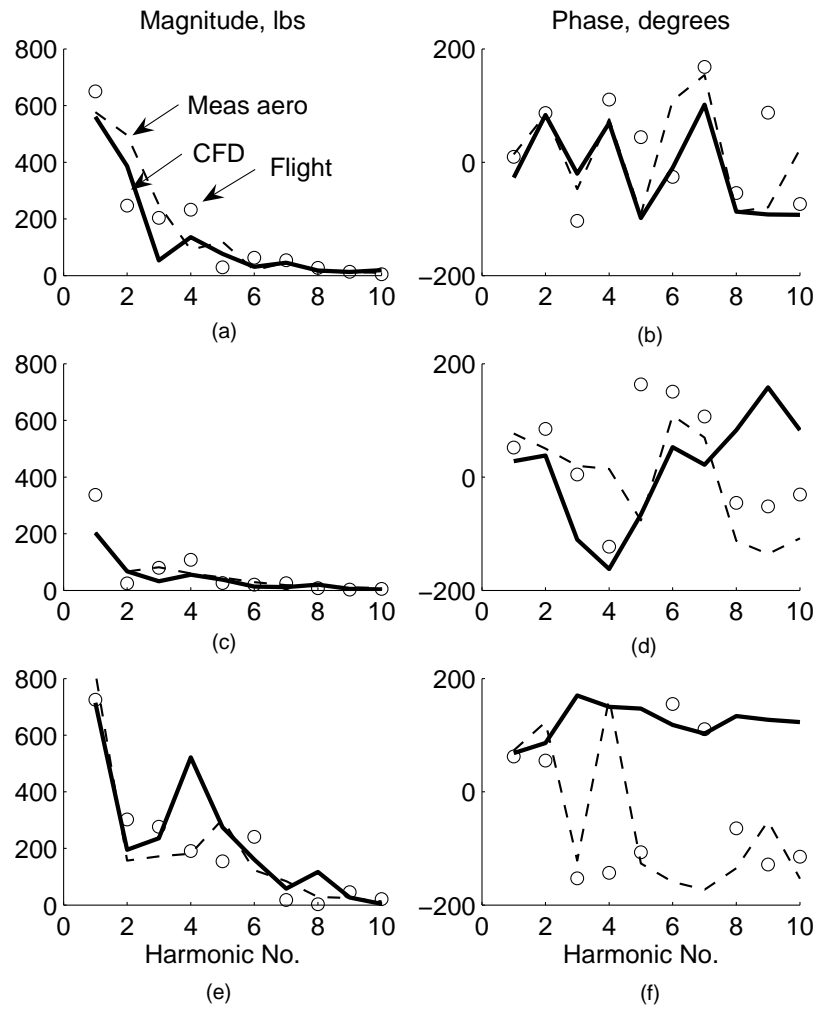


Figure 34: Measured and predicted pitch link load harmonics (1-10/rev) at the three critical flight conditions; (a,b)-High speed C8534, (c,d)-Low speed C8513, (e,f)-Stall C9017; Predictions using CFD/CSD compared with measured airloads